Monthly Notices
of the
ROYAL ASTRONOMICAL SOCIETY

MNRAS **488,** 3076–3088 (2019)
Advance Access publication 2019 July 11

doi:10.1093/mnras/stz1909

Supergranular turbulence in the quiet Sun: Lagrangian coherent structures

Abraham C.-L. Chian,[1,2,3,4★] Suzana S. A. Silva[4★] Erico L. Rempel,[3,4★] Milan Gošić,[5,6] Luis R. Bellot Rubio,[7] Kanya Kusano,[2] Rodrigo A. Miranda[8,9] and Iker S. Requerey[10]

[1]*School of Mathematical Sciences, University of Adelaide, Adelaide, SA 5005, Australia*
[2]*Institute for Space-Earth Environmental Research, Nagoya University, Furo-cho, Chikusa-ku, Nagoya 464-8601, Japan*
[3]*National Institute for Space Research (INPE), PO Box 515, São José dos Campos, SP 12227-010, Brazil*
[4]*Institute of Aeronautical Technology (ITA), World Institute for Space Environment Research (WISER), São José dos Campos, SP 12228-900, Brazil*
[5]*Lockheed Martin Solar and Astrophysics Laboratory, Palo Alto, CA 94304, USA*
[6]*Bay Area Environmental Research Institute, Moffett Field, CA 94035, USA*
[7]*Instituto de Astrofísica de Andalucía (CSIC), Apdo. de Correos 3004, E-18080 Granada, Spain*
[8]*UnB-Gama Campus, University of Brasília (UnB), Brasília DF 70910-900, Brazil*
[9]*Plasma Physics Laboratory, Institute of Physics, University of Brasília (UnB), Brasília DF 70910-900, Brazil*
[10]*Max Planck Institute for Solar System Research, Justus-von-Liebig-Weg 3, D-37077 Göttingen, Germany*

Accepted 2019 July 1. Received 2019 June 27; in original form 2019 April 17

ABSTRACT

The quiet Sun exhibits a wealth of magnetic activities that are fundamental for our understanding of solar magnetism. The magnetic fields in the quiet Sun are observed to evolve coherently, interacting with each other to form prominent structures as they are advected by photospheric flows. The aim of this paper is to study supergranular turbulence by detecting Lagrangian coherent structures (LCS) based on the horizontal velocity fields derived from *Hinode* intensity images at disc centre of the quiet Sun on 2010 November 2. LCS act as transport barriers and are responsible for attracting/repelling the fluid elements and swirling motions in a finite time. Repelling/attracting LCS are found by computing the forward/backward finite-time Lyapunov exponent (FTLE), and vortices are found by the Lagrangian-averaged vorticity deviation method. We show that the Lagrangian centres and boundaries of supergranular cells are given by the local maximum of the forward and backward FTLE, respectively. The attracting LCS expose the location of the sinks of photospheric flows at supergranular junctions, whereas the repelling LCS interconnect the Lagrangian centres of neighbouring supergranular cells. Lagrangian transport barriers are found within a supergranular cell and from one cell to other cells, which play a key role in the dynamics of internetwork and network magnetic elements. Such barriers favour the formation of vortices in supergranular junctions. In particular, we show that the magnetic field distribution in the quiet Sun is determined by the combined action of attracting/repelling LCS and vortices.

Key words: chaos – magnetic fields – turbulence – Sun: granulation – Sun: photosphere.

1 INTRODUCTION

The solar photosphere is permeated by convection cells, called granules, with a typical spatial scale of ∼1 Mm and a lifetime of a few minutes. On scales larger than granules, there is supergranulation, which is a complex non-linear dynamical phenomenon taking place in the solar photosphere that exhibits a cellular flow pattern with a typical horizontal scale of ∼30–35 Mm, a lifetime of ∼24–48 h, a strong horizontal flow velocity of ∼300–400 m s^{-1}, and a weaker vertical velocity of ∼20–30 m s^{-1} (Rincon & Rieutord 2018). The origin of supergranulation can be attributed to thermal magnetoconvection such as magnetized Raleigh–Bénard convection or large-scale instabilities, inverse cascades, and collective interactions related to turbulent convection (Hotta, Iijima & Kusano 2019).

★ E-mail: abraham.chian@gmail.com (ACLC); suzana.seas@gmail.com (SSAS); rempel@ita.br (ELR)

The supergranulation is a fundamental feature of quiet and active regions of the Sun which are composed of network (NE) and internetwork (IN) areas (Bellot Rubio & Orozco Suárez 2019). The photospheric NE outlines the supergranular cell boundaries, whereas the IN represents the interior of supergranular cells. The NE has strong fields of ∼1 kG (Stenflo 1973), whereas the IN has weaker fields of ∼1 hG (Orozco Suárez et al. 2007a,b). The IN consists of mixed-polarity magnetic elements which are advected by supergranular flows from the inner parts of a supergranular cell toward its boundaries (Orozco Suárez, Katsukawa & Bellot Rubio 2012), thus supplying the total NE flux in ∼10 h (Gošić et al. 2014). NE magnetic elements, with a characteristic size of ∼100–300 km and a downward velocity of ∼0.5 km s^{-1}, consist of vertical kG flux tubes that expand with height (Stenflo 1973). They are very persistent and may last up to tens of hours until they are diffused either by flux dispersal or cancellation with nearby elements (Liu et al. 1994). The persistence of an NE magnetic flux tube may be related to the vortical flow surrounding the magnetic structures. Such flows are able to stabilize the flux tube by the centrifugal force of its whirly motion (Schüssler 1984), as evidenced by the event found by Attie, Innes & Potts (2009) where an NE magnetic element appears to be co-aligned with a velocity vortex and the first observation of correlated magnetic vortices and photospheric downflows by Requerey et al. (2018).

It was suggested by Stenflo (1975) that persistent vortices tend to form near locations where the laminar flow is interrupted by obstacles in fluids and plasmas, e.g. in the Earth's atmosphere persistent vortices such as tropical cyclones are formed at locations where different pressure fronts collide. In supergranular junctions, the sinks in the NE are enhanced by localized downdrafts where intense inhomogeneous magnetic fields and turbulent shearing motions produce numerous pressure fronts that interact with each other. Hence, the preferential sites in the solar photosphere for the formation of persistent velocity vortices and magnetic flux tubes are supergranular junctions where the flows from various neighbouring supergranular cells meet and interact. Some ideas of Stenflo (1975) on the transport and evolution of magnetic fields and the formation of persistent vortices in the quiet Sun have been investigated and confirmed in detail by a number of papers based on the same *Hinode* data to be analysed in this paper (Orozco Suárez et al. 2012; Giannattasio et al. 2013, 2014a,b, 2018; Gošić et al. 2014, 2016; Caroli et al. 2015; Agrawal et al. 2018; Requerey et al. 2018).

Orozco Suárez et al. (2012) showed that magnetic elements are ubiquitous across the surface of the quiet Sun. They located the centre of the supergranule cell at the position of minimum radial velocity calculated from the magnetic element tracking in the time-averaged flow map. The computed horizontal velocity field of the IN magnetic elements is mostly radial and directed from the centre of a supergranule to its boundaries with a non-constant speed. On short time-scales, the chaotic motions of magnetic elements are driven mainly by granular flows, but on long time-scales, they are driven by supergranular flows. In the NE, the combined action of inflows from neighbouring supergranules traps magnetic elements in sinks.

The transport of magnetic elements by turbulent convective flows in supergranules has been studied by a series of papers (Giannattasio et al. 2013, 2014a,b, 2018). For example, Giannattasio et al. (2014b) found that the IN magnetic elements emerging from the centre of a supergranular cell have a maximum lifetime of ∼3 h, not long enough to reach the supergranular boundaries to form the network. Note, however, that the merging of IN elements with other IN elements can extend their 'effective' lifetimes. In fact, many IN elements appear close to the NE.

Gošić et al. (2014) used an automatic feature tracking algorithm to follow the evolution of IN and NE magnetic elements. They showed that IN magnetic elements continually transfer their flux to the NE by interacting with the NE magnetic elements via the merging (cancellation) processes that add (remove) flux. Gošić et al. (2016) extended the investigations of Iida, Yokoyama & Ichimoto (2010) and Iida, Hagenaar & Yokoyama (2012) to find out how small-scale IN magnetic fields appear and disappear on the solar surface. They showed that flux disappears from the IN through fading of magnetic elements, cancellation between opposite-polarity features, and interactions with the NE patches, which converts IN elements into NE features.

Requerey et al. (2018) studied the relation between a persistent photospheric vortex flow and the evolution of an NE magnetic element at a supergranular vertex. Supergranular cells are identified as large-scale divergence structures in the flow map. At their vertices and co-spatial with an NE magnetic element, the horizontal velocity flows converge to a central point. One of these converging flows is identified as a persistent vortex during the entire 24 h time-series. It consists of three consecutive vortices with a lifetime of ∼7 h each that are seen almost at the same location. At their core, an NE magnetic element is also seen. Its evolution is strongly correlated to that of the vortices, namely, the magnetic feature is concentrated and evacuated when it is caught by the vortices and is weakened and fragmented after the whirls disappear. Such behaviour is consistent with the theoretical picture of the stabilization of a magnetic flux tube by a surrounding vortical flow (Schüssler 1984).

Most of the aforementioned investigations on the spatiotemporal evolution of supergranules were based on the cork tracking techniques. One problem with such approach is its sensitivity to the choice of the number of particles and the tracer initial positions. Hence, the results thereby obtained are limited by those choices and do not necessarily reflect the overall fluid dynamics in the region. The newly developed tool of Lagrangian coherent structures (LCS, Haller & Yuan 2000; Shadden, Lekien & Marsden 2005; Mathur et al. 2007; Haller 2015) provides a more efficient method to describe the fluid topology beyond individual particle trajectories. Due to the Lagrangian nature, LCS behave as a separatrix of particles in the fluid by forming contours to separate regions of different particle movements. Hence, LCS are distinguished material lines/surfaces that predominantly influence the neighbouring particle trajectories in a given time interval by organizing the flow into coherent patterns. There are various definitions of LCS depending on whether there is greater repulsion/attraction (hyperbolic LCS), shear (parabolic LCS), or swirling motions (elliptic LCS) of particles in the fluid for the considered time interval. In this paper, we focus on the investigation of hyperbolic repelling/attracting LCS and elliptic LCS in the solar photosphere.

The non-linear dynamics tools of LCS have been applied successfully to study turbulence in terrestrial atmosphere (Rutherford, Dunkerton & Montgomery 2015), jovian atmosphere (Hadjighasem et al. 2017), ocean (Beron-Vera et al. 2018), nuclear fusion (Padberg et al. 2007; Borgogno et al. 2011), and astrophysical plasmas (Rempel, Chian & Brandenburg 2011, 2012; Rempel et al. 2013, 2017, 2019; Yeates, Hornig & Welsch 2012; Chian et al. 2014; Silva et al. 2018). A series of papers applied the technique of finite-time Lyapunov exponent (FTLE) to detect hyperbolic LCS in numerical simulation of magnetohydrodynamic turbulence in ABC dynamo (Rempel et al. 2011, 2012, 2017), α^2 mean-field dynamo (Rempel et al. 2011, 2013), and large-scale dynamo in turbulent compressible convection with uniform horizontal shear

and rotation (Chian et al. 2014). In particular, Falessi, Pegoraro & Schep (2015) applied a rigorous definition of LCS as the most repulsive or attractive material line introduced by Haller (2011) to study magnetic reconnection in plasmas and compared their results with the findings of Borgogno et al. (2011) based on the FTLE.

Recently, a number of papers applied the techniques of LCSs to analyse space observation of photospheric flows (Yeates et al. 2012; Chian et al. 2014; Rincon & Rieutord 2018; Silva et al. 2018). Yeates et al. (2012) used *Hinode* observation of a plage in the solar active region AR 10930 to study the hyperbolic repelling LCS by computing the forward FTLE (f-FTLE). They demonstrated that the network of quasi-separatrix layers (Démoulin et al. 1996) in the magnetic field corresponds to the repelling LCS, and showed how to infer the build-up of magnetic gradients in the solar corona directly from the photospheric horizontal velocity by calculating the squashing factor without recourse to magnetic field extrapolation. Chian et al. (2014) used the same data set of Yeates et al. (2012) to compute the backward FTLE (b-FTLE) and demonstrate that the network of high magnetic flux concentration in the intergranular lanes corresponds to the hyperbolic attracting LCS in the plage. Rincon & Rieutord (2018) presented nice illustrations of FTLEs for the global distribution of 24-h f-FTLE of solar surface flows using the *Solar Dynamics Observatory* (SDO) data of the quiet Sun and the local distribution of f-FTLE and b-FTLE of solar surface flows for a supergranular region using *Hinode* data. Silva et al. (2018) applied the technique of Haller et al. (2016) to detect objective velocity vortices in a supergranular region of the quiet Sun for a 15-min *Hinode* data set.

The aim of this paper is to use a 7-h sequence of high-resolution quiet-Sun observations from the *Hinode*/NFI (Narrowband Filter Imager) on 2010 November 2 to study LCS in supergranular turbulence. In contrast to the aforementioned papers which carried out the studies of hyperbolic and elliptic LCS separately, we perform for the first time a unified analysis of hyperbolic and elliptic LCS in astrophysical plasmas. Our unified study of three types of transport barriers reveals that the Lagrangian centres of a network of neighbouring supergranular cells are interconnected by ridges of the repelling LCS, which act as the transport barriers that facilitate the formation of vortices and the concentration of strong magnetic fields in the valleys of the repelling LCS. In addition, our analysis reveals that the ridges of the attracting LCS expose the locations of the sinks of photospheric flows at supergranular junctions, which are the preferential sites for the formation of elliptic LCS such as persistent vortices. Thus, our results give a strong support for the theory and observation of formation of persistent vortices and concentration of intense magnetic fluxes at supergranular junctions.

The outline of this paper is as follows. We unravel the Lagrangian skeleton of supergranular turbulence by detecting the hyperbolic and elliptic LCS in the quiet Sun in Section 3, based on high-resolution *Hinode* observations of solar photosphere described in Section 2. Discussions and conclusion are given in Section 4.

2 PHOTOSPHERIC FLOWS AND MAGNETIC FIELDS IN THE QUIET SUN

2.1 Photospheric flows

Our data analysis is based on the continuum intensity images at the quiet-Sun disc centre captured by the NFI onboard the *Hinode* satellite on 2010 November 2, within the framework of the Hinode Operation Plan 151 entitled 'Flux replacement in the photospheric network and internetwork', with a cadence of 90 s, a field of view of 80 arcsec × 74 arcsec, a pixel size of 0.16 arcsec, and a spatial resolution of 0.3 arcsec (Gošić et al. 2014). The horizontal velocity fields are extracted using the local correlation tracking (LCT) method (November & Simon 1988) implemented by Molowny-Horas (1994) and discussed by Requerey et al. (2018). Our *Hinode* data set was taken at the disc centre to make sure that the horizontal velocity fields computed by the LCT are really horizontal. The effects of 5-min oscillations were removed by applying a subsonic filter with 5 $\mathrm{km\,s^{-1}}$ as the cut-off. In order to test the accuracy of this method, we applied it to the *Hinode* continuum intensity images and Dopplergrams using a tracking window with an FWHM = 2.9 Mm that was averaged over the whole time sequence of 24 h. We confirmed that the mean horizontal velocity fields obtained with the continuum intensity images and the Dopplergrams are almost identical. In this paper, we will study supergranular turbulence using time sequences of continuum intensity images with a 2-h time average (Requerey et al. 2018).

In Fig. 1(a), the black arrows display the mean horizontal velocity field for 7-h interval from 16:46:26 UT to 23:46:34 UT; the background image displays the time-averaged Dopplergram of the line-of-sight velocities for the same time interval. In the centre of the map, a large supergranular cell is seen with a divergence structure of ∼35 Mm × 35 Mm, surrounded by other supergranular cells. The horizontal velocities are directed radially outward from the mean centre (marked by a brown cross where lies the local minimum of the mean horizontal velocity field) of each supergranular cell toward its boundary. In the interior of a supergranular cell, the Dopplergram is dominated by upflows, while the supergranular boundary is dominated by downflows (Requerey et al. 2018). A particularly prominent localized downflow in a supergranular vertex is marked by a black rectangle. A zoom in the flow streamlines of this area given in Fig. 1(b) shows spiraling velocity streamlines. Therefore, the dynamics of this region is affected by vortical motions during the time interval used to compute the mean velocity field. The centre of this persistent vortex with a mean diameter of ∼5 Mm is located in the centre of downdraft, which is indicative of a flow driven by the bathtub effect. Requerey et al. (2018) studied this vortical structure and showed that an NE magnetic element is detected in the magnetogram at the centre of the vortex flow, which corotates with the vortex in the counterclockwise direction. The vortex seen in the magnetogram has a diameter of ∼10 Mm which is larger than the bright point counterpart seen in the intensity map (Requerey et al. 2018). Note that flows from other nearby supergranular cells converge and interact in this area. Similar photospheric vortex flows at supergranular junctions have been detected previously by Brandt et al. (1988) and Attie et al. (2009).

In this paper, we detect hyperbolic and elliptic LCS using a time sequence of 281 frames of 2-h time-averaged horizontal velocity field deduced by LCT from the intensity maps for the green box region marked in Fig. 1(a) during an interval of 7 h from 16:46:26 UT to 23:46:34 UT. Figs 2(a) and (b) show the 2D horizontal velocity field at 16:46:26 UT and 23:46:34 UT, respectively. In Figs 2(c) and (d), we plot the corresponding 2-h time-averaged images of the line-of-sight magnetic field. The boundary of supergranular cells are given by the regions of low values of the mean horizontal velocity modulus, corresponding to the regions of high values of the mean downflow velocity in the Dopplergram of Fig. 1(a). It follows from Fig. 2 that there are considerable changes in both

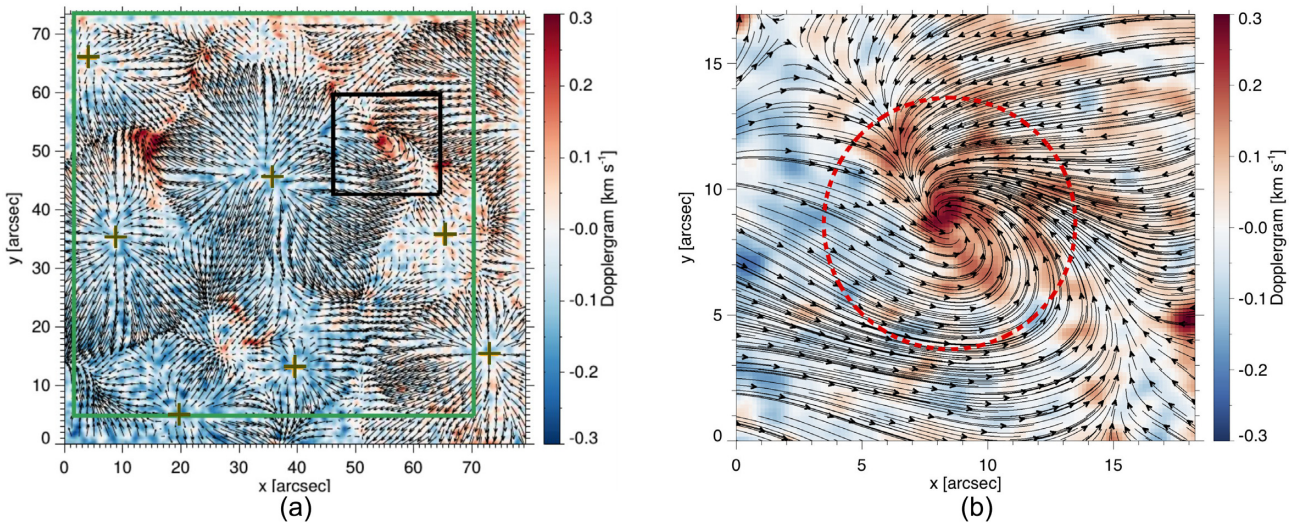

Figure 1. Horizontal photospheric flow, Dopplergram, and persistent vortex observed by *Hinode* at the disc centre of the quiet Sun on 2010 November 2. The photospheric horizontal velocity field as deduced by LCT (black arrows) and the mean Dopplergram in the background (where red and blue regions correspond to downflow and upflow areas, respectively), both time-averaged from 16:46:26 UT to 23:46:34 UT. Each brown cross denotes the mean centre of a supergranular cell determined by the local minimum of the mean horizontal velocity field. The black rectangle denotes the location of a persistent vortex. The green rectangle indicates the area where the study of LCS will be carried out in this paper. (b) An enlargement of the region marked by the black rectangle in (a), showing a persistent vortex located at a site where photospheric flows from a number of neighbouring supergranular cells meet and interact.

velocity- and magnetic-field distributions during the time interval of 7 h.

2.2 Photospheric magnetic fields

We apply the YAFTA code (Welsch & Longcope 2003) to detect and track magnetic patches in magnetograms by assigning a unique label to each feature of magnetic elements which are in constant motion advected by the photospheric flow and often interact with other features, gaining or losing flux, until they eventually disappear from the solar surface. The following dynamical processes need to be considered to track their evolution: *in situ* appearance/disappearance, merging, fragmentation, and cancellation (Gošić et al. 2014). Figs 3(a) and (b) display snapshots of magnetograms at 16:46:26 UT and 23:46:34 UT, respectively, for the photospheric region of Fig. 1(a). Pink contours outline the boundaries of supergranular cells as deduced from LCT, which separate NE and IN regions. Blue contours indicate the NE elements, and IN elements are indicated in other colours. These magnetograms show IN flux patches, many of which eventually supply flux to the NE.

The background images in Figs 3(a) and (b) show an Eulerian (snapshot) view of the magnetic flux density at (a) 16:46:26 UT and (b) 23:46:34 UT, respectively. It follows from Figs 1 and 3 that as the IN magnetic elements are advected by the radially directed outflows, from the centre to the boundary of a supergranular cell, they undergo a rich variety of dynamical processes. In particular, when IN magnetic elements reach the supergranular boundary they interact with the NE magnetic elements which allows the deposit of their flux in supergranular junctions (for more details, see Gošić et al. 2014, 2016). Furthermore, the shape and size of supergranular cells as well as the morphology and structure of the NE in supergranular junctions vary considerably in 7 h from Figs 3(a) to (b).

3 LAGRANGIAN COHERENT STRUCTURES IN SUPERGRANULAR TURBULENCE

3.1 Hyperbolic Lagrangian coherent structures

First, we determine the hyperbolic LCS in supergranular turbulence by computing the f-FTLE/b-FTLE (Shadden et al. 2005; Padberg et al. 2007; Borgogno et al. 2011; Rempel et al. 2011, 2012; Yeates et al. 2012; Rempel et al. 2013; Chian et al. 2014) of the horizontal velocity field by advecting a dense grid of 405 × 405 tracer particles over the domain of interest. Haller (2015) pointed out that the FTLE is not objective (i.e. invariant under time-dependent translations and rotations of the reference frame). Hence, the FTLE results must be handled with caution. Consider a tracer particle advected by the velocity field $\boldsymbol{u}(\boldsymbol{r}, t)$ from an initial time t_0 and solve the particle advection equation

$$\frac{\mathrm{d}\boldsymbol{r}}{\mathrm{d}t} = \boldsymbol{u}(\boldsymbol{r}, t) \tag{1}$$

over a grid of initial positions $\boldsymbol{r}_0$ until the final positions $\boldsymbol{r}(t_0 + \tau)$ are reached after a finite-time duration τ. The FTLEs of the particle trajectories for a 2D flow are calculated at each initial position $\boldsymbol{r}_0$ as

$$\sigma_{\mathrm{i}}^{t_0+\tau}(\boldsymbol{r}_0) = \frac{1}{|\tau|} \ln \sqrt{\lambda_{\mathrm{i}}}, \qquad i = 1, 2 \tag{2}$$

where λ_{i} ($\lambda_1 > \lambda_2$) are the eigenvalues of the finite-time right Cauchy–Green deformation tensor $\Delta = J^{\top}J$, in which $J = \mathrm{d}\phi_{t_0}^{t_0+\tau}(\boldsymbol{r})/\mathrm{d}\boldsymbol{r}$ is the deformation gradient, $\top$ denotes the transpose, and $\phi_{t_0}^{t_0+\tau} : \boldsymbol{r}(t_0) \rightarrow \boldsymbol{r}(t_0 + \tau)$ is the flow map for equation (1). Advecting a particle forward in time reveals the repelling LCS in the f-FTLE field, which is the source of stretching in the flow, whereas advecting a particle backward in time reveals the attracting LCS in the b-FTLE field along which particles congregate to form the observable patterns. Equation (1) is solved using a fourth-order Runge–Kutta integrator; to obtain a continuous

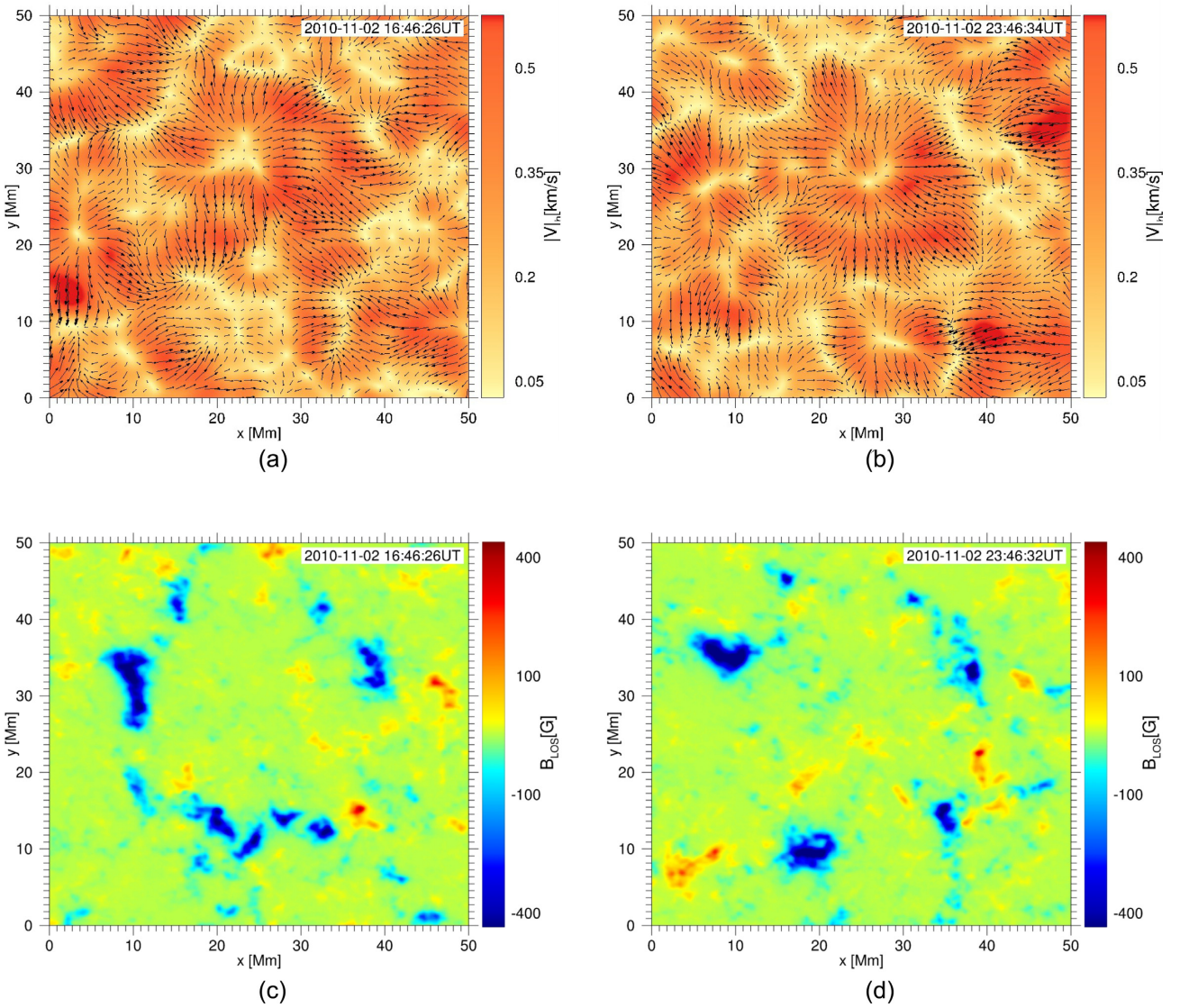

Figure 2. Horizontal velocity field and line-of-sight magnetic field. The 2-h time-averaged horizontal velocity field (black arrows) deduced by applying LCT to the intensity maps and the horizontal velocity modulus (the background image) for the green rectangle region marked in Fig. 1(a) at (a) 16:46:26 UT and (b) 23:46:34 UT. The corresponding 2-h time-averaged line-of-sight magnetic field at (c) 16:46:26 UT and (d) 23:46:34 UT.

time-varying velocity field, cubic splines are used for space and time interpolations using a discrete set of velocity field frames previously obtained with the LCT method.

Fig. 4(a) shows a 2D plot of f-FTLE for the supergranular region of Fig. 1(a) marked by the green rectangle, computed forward in time using the sequence of 281 frames of the horizontal velocity field from 16:46:26 UT to 23:46:34 UT. The white crosses mark the locations of the time-dependent Lagrangian centres of supergranular cells characterized by local maxima of f-FTLE. The brown crosses mark the locations of the Eulerian centres of supergranular cells seen in Fig. 1(a) for the sake of comparison between Eulerian and Lagrangian methods. Thin ridges of large positive f-FTLE in Fig. 4(a) represent the locally strongest repelling material lines which exert the most influential impact on the diverging transport of supergranular flows in the given time interval. These are interspersed by regions of negative f-FTLE, indicating converging trajectories. Yeates et al. (2012) and Chian et al. (2014) demonstrated that f-FTLE is closely related to the squashing Q-factor, which identifies the most likely locations for the occurrence of magnetic reconnection (Démoulin et al. 1996; Inoue, Hayashi & Kusano 2016). Hence, the ridges of f-FTLE indicate the preferential sites for magnetic elements to interact and reconnect.

Fig. 4(b) shows the corresponding plot of b-FTLE for the supergranular region. In Figs 3(a) and (b), we get a rough (estimated) view of the Eulerian (snapshot) boundaries of supergranular cells at 16:46:26 UT and 23:46:34 UT, respectively. In contrast, Fig. 4(b) gives an accurate view of the complex time-dependent Lagrangian boundaries of supergranular cells. Thin ridges of large positive b-FTLE in Fig. 4(b) represent the locally strongest attracting material lines that exert the most influence on the converging transport of supergranular flows. These are interspersed by regions of negative a-FTLE, indicating diverging trajectories. Note that the b-FTLE is closely related to the Lagrangian analysis of corks (November &

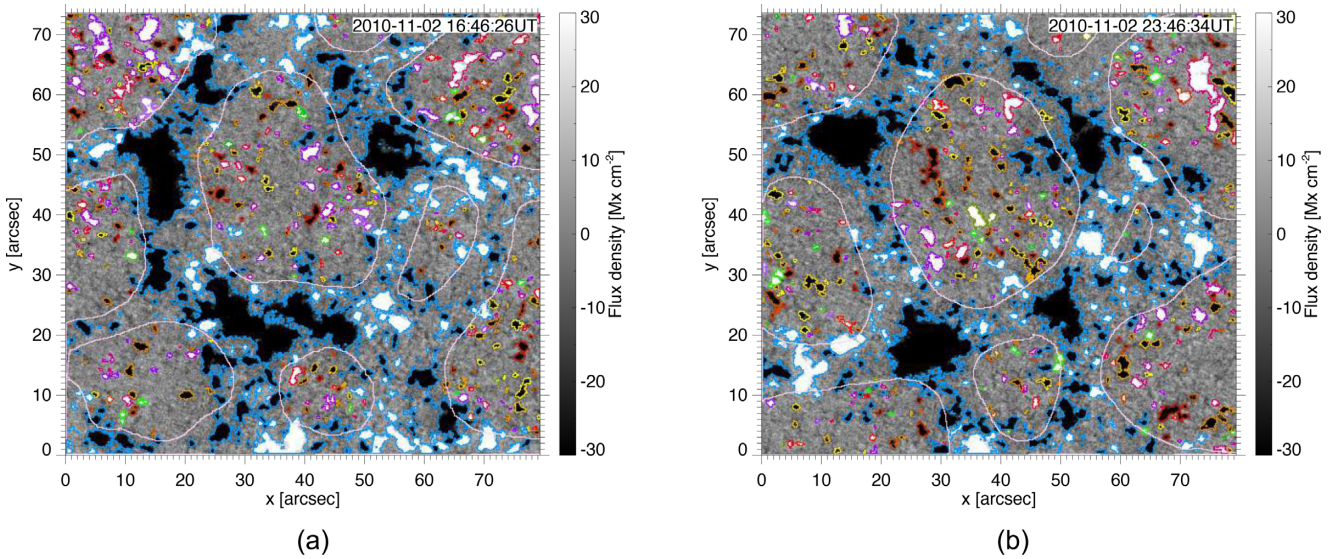

Figure 3. Individual magnetograms. The line-of-sight magnetic flux density at (a) 16:46:26 UT and (b) 23:46:34 UT. The pink contours outline the Eulerian (snapshot) boundaries of supergranular cells that separate NE and IN regions as deduced by LCT; blue contours indicate the NE magnetic elements; and IN magnetic elements are displayed in other colours.

Simon 1988; Roudier et al. 2018), but it enables us to acquire additional important information on the local rate of the flow convergence indicated by the ridges of large (positive) b-FTLE. Chian et al. (2014) established the correspondence of the network of high magnetic flux concentration to the attracting LCS, as seen in supergranular junctions. Figs 4(c) and (d) exhibit surface plots of f-FTLE and b-FTLE, respectively, which present a 3D perspective of the thin ridges of the repelling and attracting LCS. The ridges of the repelling LCS seen in 4(c) provide the transport barriers that facilitate the concentration of strong magnetic fields and formation of vortices in the valleys (i.e. regions of low-value f-FTLE) of the repelling LCS. The ridges of the attracting LCS seen in Fig. 4(d) act as the sinks for downdraft of photospheric flows that lead to vortical motions.

3.2 Elliptic Lagrangian coherent structures

The Lagrangian-averaged vorticity deviation (LAVD) is an objective method for detecting elliptic LCS (vortices) developed by Haller et al. (2016) for fluids. Rempel et al. (2017) and Silva et al. (2018) applied LAVD to detect vortices in plasmas. The LAVD field is computed by the integral

$$\mathrm{LAVD}_{t_0}^{t_0+\tau} := \int_{t_0}^{t_0+\tau} |\boldsymbol{\omega}(\boldsymbol{r}(s), s) - \langle \boldsymbol{\omega}(s) \rangle| \mathrm{d}s \qquad (3)$$

where $\boldsymbol{\omega} = \nabla \times \boldsymbol{u}$ is the vorticity, τ denotes a finite time interval, and $\langle \cdot \rangle$ denotes the instantaneous spatial average. Fluid particle trajectories are determined by solving equation (1) over a grid of initial positions $\boldsymbol{r}_0$ until the final positions $\boldsymbol{r}(t_0 + \tau)$ are reached after a finite time duration τ.

For a finite time duration $[t_0, t_0 + \tau]$, a Lagrangian vortex is defined as an evolving material domain filled with a nested family of convex tubular level surfaces of $\mathrm{LAVD}_{t_0}^{t_0+\tau}$ with outward-decreasing LAVD values. In contrast to the Eulerian methods that detect instantaneous swirl-like structures that do not convey long-term information of fluid motions, it was demonstrated that the LAVD method is capable of detecting persistent vortical flows (Haller et al. 2016; Rempel et al. 2017; Silva et al. 2018). For 2D incompressible, shearless, non-magnetized fluids, the centre of objective vortices are usually cospatial with a local maximum of the LAVD field (Haller et al. 2016). This is not necessarily true for highly compressible magnetized fluids with strong shear regions such as photospheric flows, for which we must allow some deviation from convexity to ensure that all vortex cores are captured. Moreover, Silva et al. (2018) showed that in order to avoid false vortex detection in flows with strong shear, such as supergranulations, it is necessary to apply a post-processing filter to the set of vortices detected by LAVD. The d-criterion, based on the geometry of the streamlines of the displacement vector field of fluid elements, is adopted to find vortex cores. A grid point is considered a vortex core if the displacement vectors computed from its neighbouring points indicate a clockwise or counterclockwise motion pattern. The displacement vectors are computed by advecting the neighbouring particles for a given time and subtracting their initial positions from their final positions. For details, see Silva et al. (2018). An LAVD vortex is considered a true vortex boundary if it surrounds a vortex core detected by the d-criterion.

We considered the supergranular region marked by the green rectangle in Fig. 1(a) and applied the LAVD method together with the d-parameter to detect coherent objective vortices. Figs 5(a) and (b) show two examples of 2D plots of the LAVD field computed from 20:16 UT to 20:31 UT for $\tau = 15$ min and from 20:46 UT to 21:46 UT for $\tau = 60$ min, respectively. The boundary of each Lagrangian vortex is indicated by a magenta line, denoting the outermost closed (approximately convex) line of LAVD. It is worth mentioning that the parameter τ is not a measure of the vortex lifetime; rather, it is the finite time interval for computing LAVD. Physically, τ is the time for which the fluid elements are trapped within the LAVD contour following swirl-like motions. Figs 5(c) and (d) exhibit 3D surface plots of Figs 5(a) and (b), respectively, presenting a 3D perspective of Lagrangian vortices detected. The centre of a Lagrangian vortex is given by the location of the centre of the spiral streamlines of the displacement vector field that obeys the d-criterion (Silva et al. 2018). The LAVD contour represents the

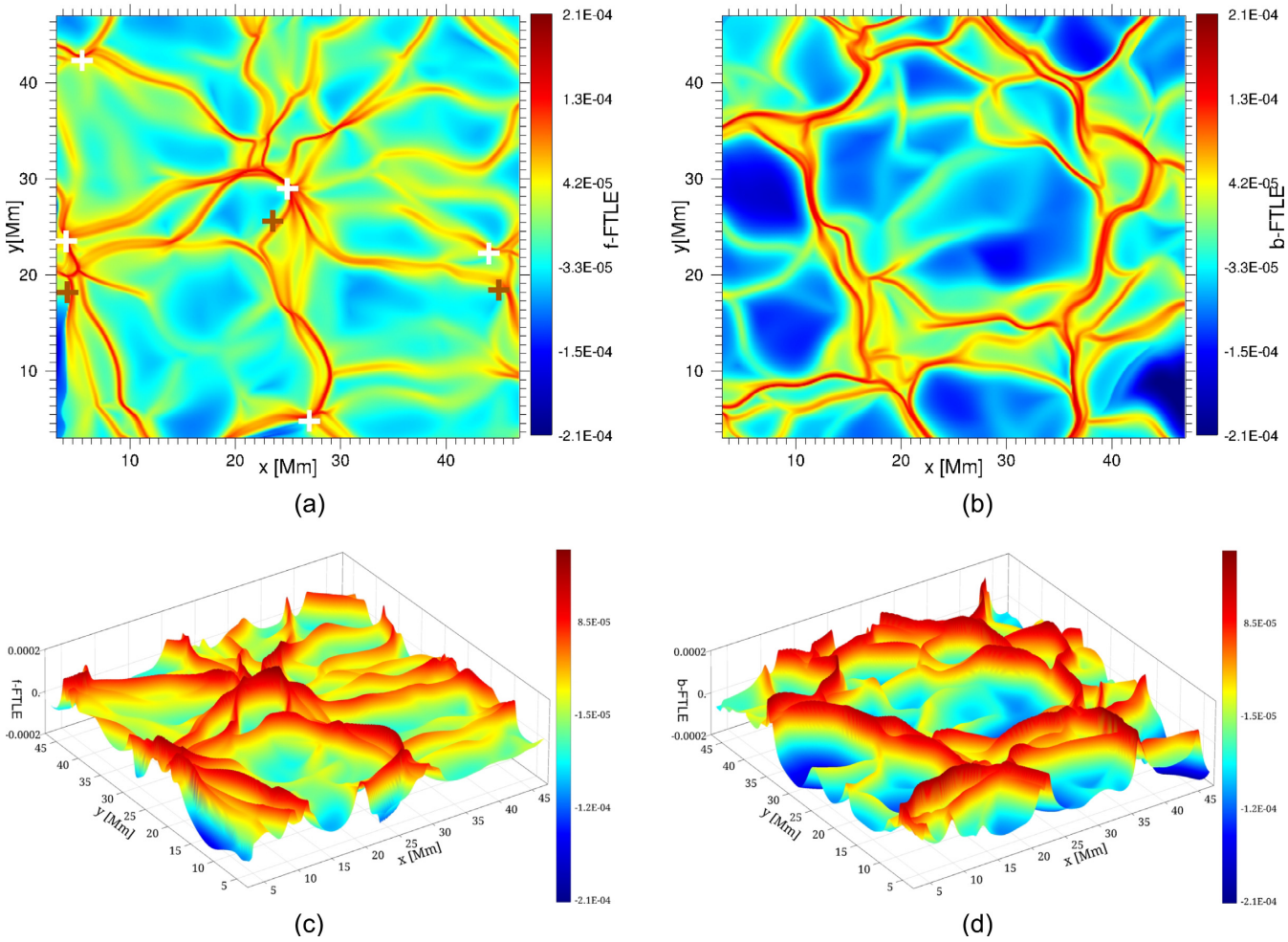

Figure 4. Hyperbolic repelling and attracting LCS of supergranular turbulence in the time interval from 16:46:26 UT to 23:46:34 UT on 2010 November 2. (a) 2D plot of the f-FTLE computed for $t_0 = 16{:}46{:}26$ UT and $\tau = +7$ h. (b) 2D plot of the b-FTLE computed for $t_0 = 23{:}46{:}34$ UT and $\tau = -7$ h. (c) 3D surface plot of the f-FTLE of (a). (d) 3D surface plot of the b-FTLE of (b). The white crosses in (a) indicate the Lagrangian centres of supergranular cells determined by the local maxima of the f-FTLE. Lagrangian centres of nearby supergranular cells are interconnected by ridges of the f-FTLE. Lagrangian boundaries of supergranular cells are given by the ridges of the b-FTLE. The ridges in (c) and (d) are interspersed by valleys dominated by converging flows (c) and diverging flows (d), respectively. In (a) the brown crosses from Fig. 1(a) are overlaid to compare the detection of supergranules using the Eulerian versus Lagrangian methods.

material line where all the particles experience the same intrinsic dynamic rotation (Haller et al. 2016).

In Figs 6(a) and (b), we plot the boundary (denoted by a magenta line) of all Lagrangian vortices detected by LAVD and d-criterion using a sliding window with a duration τ during the 7-h interval from 16:46:26 UT to 23:46:34 UT, for (a) $\tau = 15$ min and (b) $\tau = 60$ min, respectively, superposed by the f-FTLE computed from 16:46:26 UT to 23:46:34 UT given by Fig. 4(a). In Figs 6(c) and (d), the same vortex boundaries as in Figs 6(a) and (b) are plotted and superposed by the b-FTLE computed from 23:46:34 UT to 16:46:26 UT given by Fig. 4(b). We can see that the elliptic LCS are distributed along the Lagrangian supergranular boundaries.

The centre (denoted by a magenta cross) of all detected Lagrangian vortices are displayed in Figs 7(a) and (b). The background image displays the horizontal velocity modulus time averaged from 16:46:26 UT to 23:46:34 UT. In Figs 7(c) and (d), the same Lagrangian vortex centres as in Figs 7(a) and (b) are plotted and superposed by a background image that displays the line-of-sight magnetic field time averaged from 16:46:26 UT to 23:46:34 UT.

The total number of Lagrangian vortices detected from 16:46:26 UT to 23:46:34 UT for $\tau = 15$ min is 50, as seen in Figs 7(a) and (c); the total number of Lagrangian vortices detected for $\tau = 60$ min is 9, as seen in Figs 7(b) and (d). Note that Fig. 6 does not show all vortices detected because we have to reduce the photospheric area of Fig. 6 in view of large numerical errors in the edge region of the computed LAVD and FTLE fields, as passive particles are advected toward the domain boundaries.

4 DISCUSSIONS AND CONCLUSION

An example of Eulerian vortex located at supergranular junctions is given in Fig. 1 where flows from several nearby supergranular cells collide and interact, leading to the formation of a persistent vortex associated with photospheric swirling flows and concentration of strong magnetic fluxes. The mean Dopplergram obtained by averaging over a 7-h duration of the high-resolution

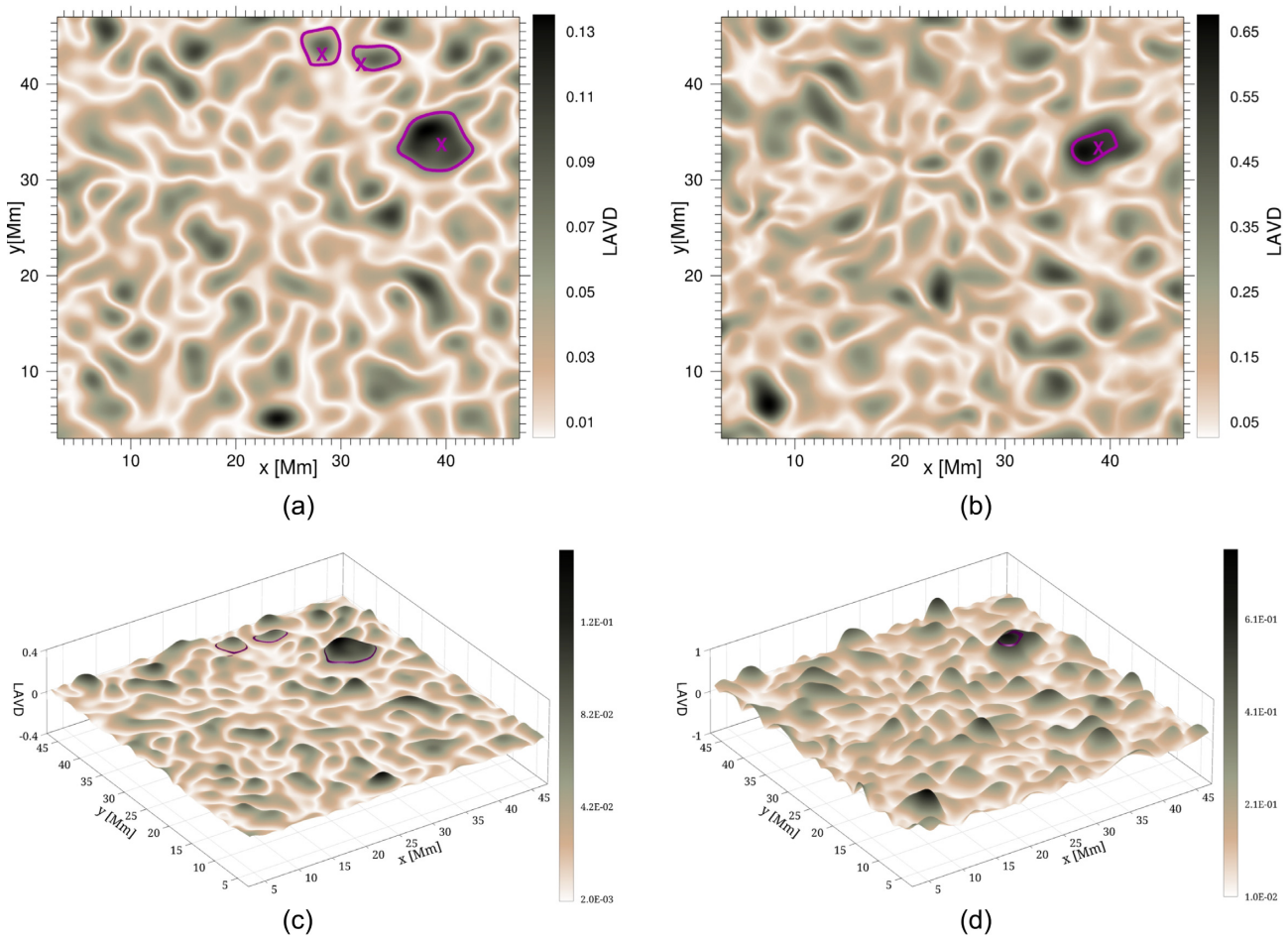

Figure 5. Elliptic LCS of supergranular turbulence where the magenta line (cross) denotes the boundary (centre) of each Lagrangian vortex. (a) and (b) 2D plot of LAVD for the supergranular region marked by the green rectangle in Fig. 1(a) computed from 20:16 UT to 20:31 UT (a) using $\tau = 15$ min, and from 20:46 UT to 21:46 UT (b) using $\tau = 60$ min. (c) and (d) 3D surface plot of LAVD for Figs 5(a) and (b), respectively.

Hinode data set shows that the interior of a supergranular cell is dominated by upflows, whereas the supergranular boundaries are dominated by downflows; the horizontal velocities driven by turbulent magnetoconvection are directed radially outward from the mean centre of a supergranular cell, given by the local minimum of the mean horizontal velocity field, toward supergranular junctions. We applied in this paper the techniques of LCS to improve our understanding of the dynamics and structures of supergranular turbulence by demonstrating how the magnetic field distribution in the quiet Sun is formed by the combined action of transport barriers provided by repelling/attracting LCS and objective vortices.

In this paper, we chose the average lifetime of 7 h of the persistent vortices detected by Requerey et al. (2018) to probe in detail the relation between elliptic LCS (computed by LAVD) and hyperbolic LCS (computed by FTLE). Note that FTLE is dependent on the choice of the integration time (see fig. 5 of Yeates et al. 2012 and fig. 3 of Chian et al. 2014), as illustrated in Fig. 8, where we plot FTLEs for two different integration times, $\tau = 7$ h (a) and (c), and 2 h (b) and (d). In Fig. 8, we only plot positive values of FTLEs with a threshold of 0.00015 to emphasize the ridges of hyperbolic LCS. The background image is the line-of-sight magnetic field averaged over the respective time interval τ. Fig. 8 shows that as the integration time increases, some structures persist and become more sharply defined. These structures can be considered most influential over time. The structures that fail to persist as the integration time is increased can be considered to be due to more transient (short-lived) flow features.

Our LCS analysis is based on the 2-h time-averaged horizontal velocity field deduced by LCT from *Hinode*/NFI continuum intensity images, exemplified by Fig. 2 for the initial and final frames of a 7-h continuous *Hinode* observation at disc centre. The repelling LCS, obtained by computing the f-FTLE for duration of 7 h, shown in Fig. 4, identifies the locally strongest repelling material lines which exert the most impact on the diverging transport of supergranular flows, thus indicating the source regions of magnetic elements. The Lagrangian centre of the supergranule can be defined as the local maximum of the f-FTLE field, as it marks the region where particles diverge the most during the considered time interval. We demonstrated that the interior of supergranules is dominated by the repelling material lines which act as transport barriers within IN regions to prevent mixing of IN magnetic patches across them. The Lagrangian centres of neighbouring supergranular cells are interconnected by ridges of the repelling LCS, as seen in Fig. 4. Since the f-FTLE is closely linked to the squashing Q-factor (Démoulin et al. 1996; Yeates et al. 2012; Chian et al. 2014; Inoue et al. 2016), the repelling LCS also identify the most likely sites for the occurrence of element–element interactions

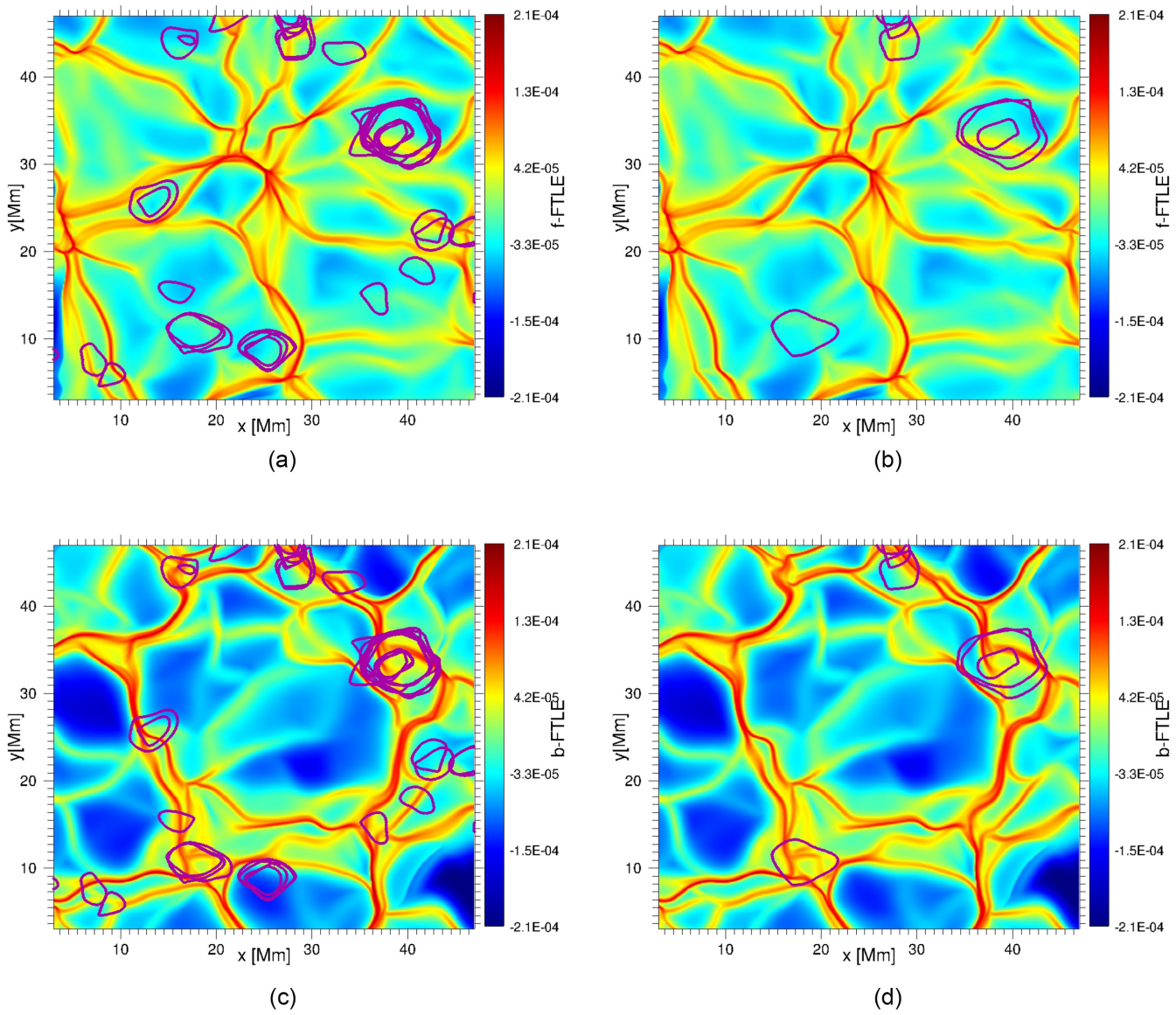

Figure 6. Superposition of elliptic and hyperbolic LCSs on 2010 November 2. (a, b) Superposition of all Lagrangian vortices detected by LAVD and the d-criterion for the time interval from 16:46:26 UT to 23:46:34 UT, using a sliding window of (a) $\tau = 15$ min and (b) $\tau = 60$ min, respectively, with the f-FTLE given by Fig. 4(a). (c, d) Superposition of all Lagrangian vortices detected by LAVD for the time interval from 16:46:26 UT to 23:46:34 UT, using a sliding window of (c) $\tau = 15$ min and (d) $\tau = 60$ min, respectively, with the b-FTLE given by Fig. 4(b). The magenta line denotes the boundary of each Lagrangian vortex.

such as the cancellation and merging events seen in *Hinode*/NFI magnetograms.

The attracting LCS obtained by computing the b-FTLE for a duration of 7 h, shown in Fig. 4, display thin ridges of large positive b-FTLE, representing the locally strongest attracting material lines which exert the most impact on the converging transport of supergranular flows. Therefore, they act as the Lagrangian supergranular boundaries which identify the preferential sites of photospheric downdrafts; the attracting LCS are cospatial with the photospheric network of strong magnetic flux concentration, which confirms the trapping of magnetic elements in the NE region observed by Orozco Suárez et al. (2012). The attracting material lines provide the transport barriers between the supergranules, indicating that the mixing of IN elements is restrained to the NE region of supergranule as demonstrated by Gošić et al. (2014), who applied an automatic feature tracking algorithm to follow the evolution of IN and NE magnetic elements. They showed that the IN magnetic elements continually transfer their flux to the NE by interacting with the NE magnetic elements via the merging (cancellation) processes that add (remove) flux. In contrast to the simple picture of supergranular boundaries given by the Eulerian magnetograms in Fig. 3, we see in Fig. 4 that the Lagrangian supergranular boundaries are very complex, resulting from the non-linear interactions between supergranular cells.

By superposing the boundary of all Lagrangian vortices detected during 7 h with the b-FTLE in Fig. 6, we see that the Lagrangian vortices are mostly located in the high-value regions of the b-FTLE, where the ridges of the attracting LCS provide the sinks for photospheric flows. Therefore, most of those vortices are very likely to be a consequence of the bathtub effect. Physically, the

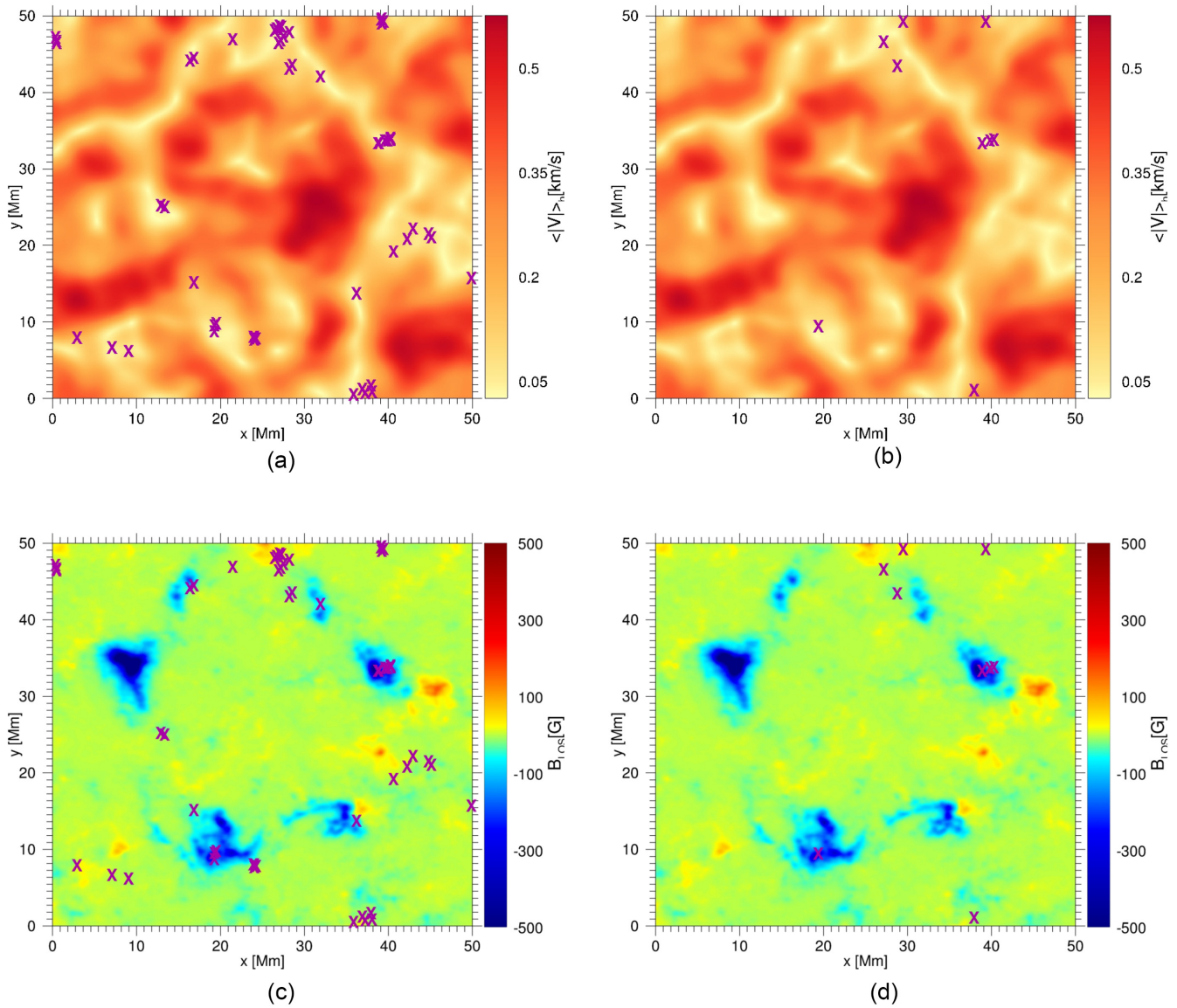

Figure 7. Superposition of Lagrangian vortex centres with the mean horizontal velocity modulus and the mean line-of-sight magnetic field for the time interval from 16:46:26UT to 23:46:34 UT on 2010 November 2. (a, b) Superposition of all Lagrangian vortex centres detected by LAVD and the d-criterion using a sliding window of (a) $\tau = 15$ min and (b) $\tau = 60$ min, respectively, with a background image that displays the horizontal velocity modulus time-averaged from 16:46:26 UT to 23:46:34 UT. (c, d) Superposition of all Lagrangian vortex centres detected by LAVD and the d-parameter using a sliding window of (c) $\tau =$ 15 min and (d) $\tau = 60$ min, respectively, with a background image that displays the line-of-sight magnetic field time averaged from 16:46:26 UT to 23:46:34 UT. The magenta cross denotes the centre of each Lagrangian vortex.

contours obtained for the vortices mean that for the time interval considered the fluid elements within the contour are trapped in that region. Therefore, magnetic elements patches tend to be trapped by the vortices which cause the magnetic field intensity to increase. Once the vortex ceases to exist, the magnetic elements will be free to go to other regions, leading to NE magnetic flux reorganization (e.g. merging and cancellation) as observed by Requerey et al. (2018). By superposing the centre of all Lagrangian vortices detected with the 7-h time-averaged horizontal velocity field and line-of-sight magnetic field in Fig. 7, we confirm that the supergranular junctions are the preferential sites for the concentration of intense magnetic flux as well as the formation of Lagrangian vortices and associated kG magnetic flux tubes. In particular, Fig. 7 confirms the detection of the persistent vortex that appears in the black rectangle region of Fig. 1(a).

The repelling hyperbolic LCS create transport barriers within supergranular cells and from one cell to other cells, yielding observable physical impact on the movement of magnetic elements, as revealed by Figs 8(a) and (b), which display a superposition of the f-FTLE with the time-averaged line-of-sight magnetic field for $\tau =$ 7 h (a) and 2 h (b), respectively. Figs 8(a) and (b) are compatible with the idea that the IN magnetic elements advected by turbulent convective flow diverge preferentially along the repelling LCS until they reach the Lagrangian boundaries of supergranular cells, then converge preferentially to the attracting LCS shown in Figs 8(c) and (d). It follows from Fig. 8(a) that the patches of intense magnetic

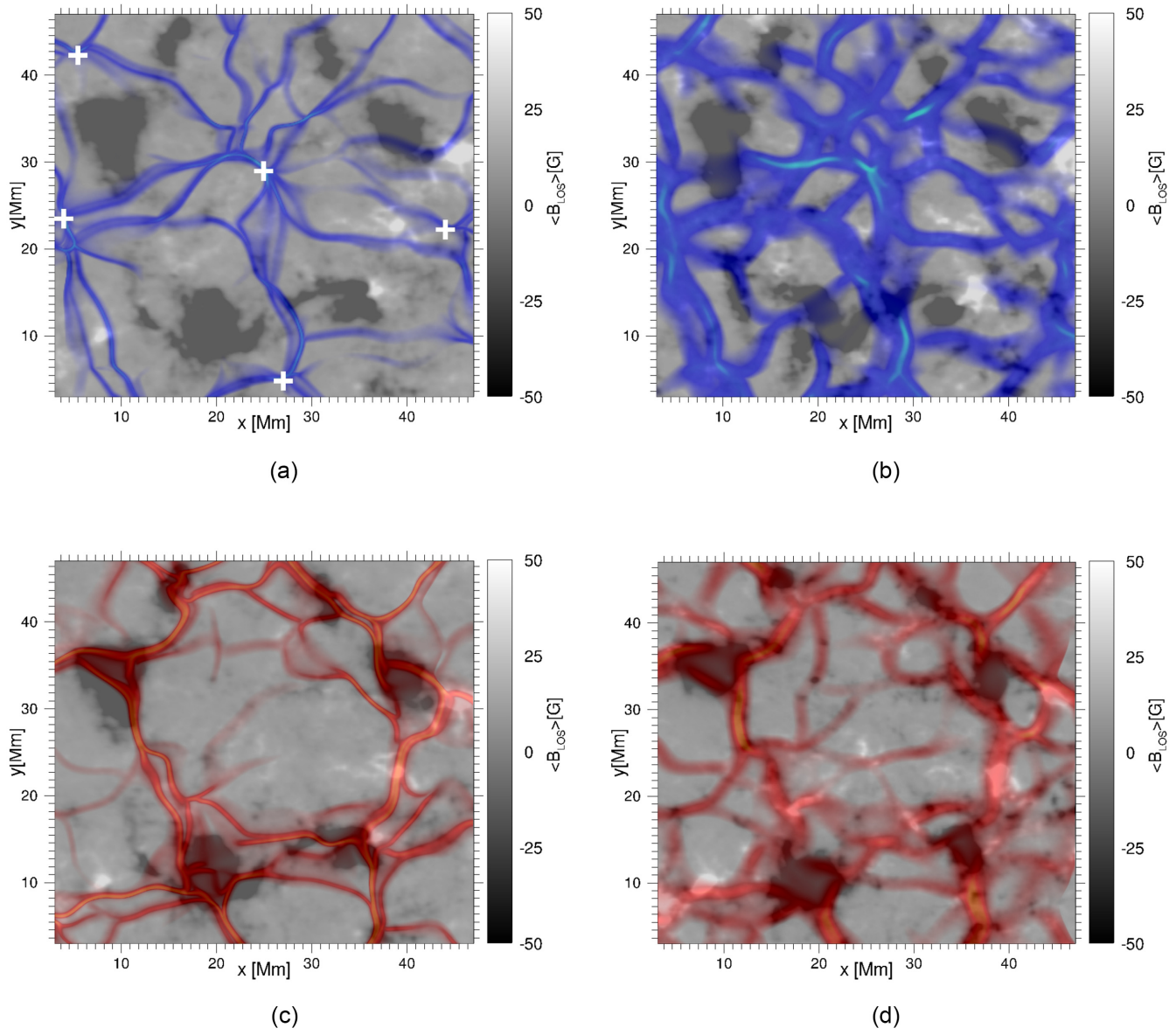

Figure 8. Hyperbolic LCSs and mean magnetograms. Repelling LCS (blue line) obtained by computing the f-FTLE (a) from $t = 16{:}46{:}26$ UT to 23:46:34 UT and (b) from $t = 16{:}46{:}26$ UT to 18:46:26 UT, respectively. Attracting LCS (orange line) obtained by computing the b-FTLE (c) from 23:46:34 UT to 16:46:26 UT and (d) from 23:46:34 UT to 21:46:34 UT, respectively. The background images show the respective time-averaged magnetograms of the line-of-sight magnetic field for the time interval used to compute the hyperbolic LCSs. The white cross marks the Lagrangian centre of supergranular cells. The repelling and attracting LCS are plotted with a threshold of 0.00015, the lighter the colour the higher the value of FTLE.

fields in supergranular junctions are bounded by the ridges of high positive value f-FTLE fields. In particular, Fig. 8(a) shows clearly that as the magnetic elements diverge along the repelling LCS, they tend to create magnetic voids in the regions where they cross the attracting hyperbolic LCS at the supergranular junctions shown in Fig. 8(c).

Rieutord et al. (2000) applied the cork technique of Simon & Weiss (1989) to a set of 3-h velocity field of the quiet-Sun photosphere recorded at Pic du Midi Observatory to confirm the view that a 3-h time average of horizontal flows can show the supergranular scale. They integrated the trajectories of corks, initially uniformly distributed, and plotted the final spatial distribution of the corks after 3 h which demonstrated the coincidence between the regions with a high density of corks and the positions of network bright points. In this paper, we identify the supergranular pattern using the b-FTLE by first integrating the particle trajectories, initially uniformly distributed, backward in time for a finite time interval, and then plot the maximum b-FTLE at the initial position of each particle. Fig. 8(d) suggests that the LCS technique is capable of showing the supergranular scale for an integration time of 2 h which is shorter than the cork results of 3 h (Rieutord et al. 2000), albeit a longer integration time improves significantly the viewing of the supergranular pattern due to the enhancement of the ridges as seen in Fig. 8(c). Note that in addition to the ability of the b-FTLE of providing a novel method to identify the supergranular patterns, we showed in Figs 4(b) and (d) that the ridges of the attracting LCS

provide a quantitative measure of the rate of convergence of the photospheric flows. This important information is missing in the cork technique.

Vortex flows are ubiquitous in the solar surface convection, with lifetimes varying from a few minutes to a few hours (Steiner & Rezaei 2012). This is consistent with the multiscale nature of photospheric turbulence, where vortices with a wide range of spatial and temporal scales are expected. Our 7-h long-duration statistical study of Lagrangian vortices shows that the number of vortex detection depends on the integration time during LAVD computations. For the integration time on the order of minutes, characteristic lifetime of granules, a large number of vortices is detected (Figs 6a and c, 7a and c). On the integration time on the order of hours, characteristic lifetime of supergranules, a small number of persistent vortices is detected (Figs 6b and d, 7b and d) which are related to photospheric downflows in the supergranular junctions. The short-lived vortices cannot be found with the LAVD method using long-time integrations because when they are destroyed, the particles that were swirling inside the vortex spread away toward regions with smaller vorticity deviation, thus decreasing the integrand in equation (3). In our experience with the present data set, this often happens when the vortex centres interact with the flow regions with a strong shear.

In Figs. 8(c) and (d), we demonstrated that the attracting LCS are cospatial with the concentration of magnetic fluxes in the supergranular junctions, giving further support for the previous results of Chian et al. (2014) for the intergranular lanes. Fig. 8(d) shows that the magnetic field pattern in supergranular junctions appears for an integration time of 2 h. However, the coincidence of the a-FTLE with the network of magnetic fluxes improves considerably for a longer integration time as seen in Fig. 8(c).

The study of supergranulation is relevant for understanding solar dynamo, coronal heating, and eruption. In this paper, we applied the LCS approach to deepen our understanding of the photospheric flows in the quiet-Sun supergranulations, confirming that LCS provide a powerful tool to determine the transport properties of photospheric flows and the complex dynamics of solar magnetic fields (Aschwanden et al. 2018; Rincon & Rieutord 2018; Roudier et al. 2018). Our analysis revealed that the supergranular turbulence is governed by hyperbolic and elliptic LCS, demonstrating that supergranulation-scale convection plays a key role in the non-linear dynamics of local and global solar magnetic fields at the interface between solar interior and atmosphere. The conclusions of this paper are based on a 7-h LCS data analysis for a photospheric region of 50 Mm $\times$ 50 Mm. Future works can apply this technique to different temporal and spatial scales of quiet- and active Sun. In conclusion, the detection of LCSs in supergranular turbulence can deepen our understanding of the non-linear dynamics and complex structures of the photosphere, as well as improve our ability to monitor and predict solar and astrophysical eruptive events such as flares and coronal mass ejections.

ACKNOWLEDGEMENTS

This work is dedicated to the 160th anniversary of the first report by Richard Christopher Carrington (a graduate of Trinity College, Cambridge) of a solar superflare on 1859 September 1 and its relation to a major geomagnetic storm, published in MNRAS 20, 13, 1859. The data used here were acquired in the framework of the *Hinode* Operation Plan 151 *'Flux replacement in the solar network and internetwork.'* We thank the *Hinode* Chief Observers for the efforts they made to accommodate our demanding observations. *Hinode* is a Japanese mission developed and launched by Institute of Space and Astronautical Science/Japan Aerospace Exploration Agency (ISAS/JAXA), with National Astronomical Observatory of Japan (NAOJ) as a domestic partner and National Aeronautics and Space Administration (NASA) and Science and Technology Facilities Council (STFC, UK) as international partners. It is operated by these agencies in co-operation with European Space Agency (ESA) and Norwegian Space Centre (NSC, Norway). SSAS acknowledges financial support from agency Coordenação de aperfeiçoamento de Pessoal de nível Superior (CAPES 88882.316962/2019-01, Brazil). ELR acknowledges financial support from Conselho Nacional de Desenvolvimento Científico e Tecnológico (CNPq, Brazil), partial financial support from CAPES (Brazil) and from Fundação de Amparo à Pesquisa de São Paulo (FAPESP, Brazil). LBR acknowledges financial support from the Spanish Ministerio de Ciencia, Innovación y Universidades through grant RTI2018-096886-B-C51, including a percentage from European Regional Development Fund (FEDER), and through the 'Center of Excellence Severo Ochoa' award to the Instituto de Astrofísica de Andalucía (SEV-2017-0709). We are grateful to the reviewer for constructive comments to improve our manuscript.

REFERENCES

Agrawal P., Rast M. P., Gošić M., Bellot Rubio L. R., Rempel M., 2018, ApJ, 854, 118
Aschwanden M. J., Gošic M., Hurlburt N. E., Scullion E., 2018, ApJ, 866, 73
Attie R., Innes D. E., Potts H. E., 2009, A&A, 493, L13
Bellot Rubio L., Orozco Suárez D., 2019, Living Rev. Sol. Phys., 16, 1
Beron-Vera F. J., Olascoaga M. J., Wang Y., Triñanes J., Pérez-Brunius P., 2018, Sci. Rep., 8, 11275
Borgogno D., Grasso D., Pegoraro F., Schep T. J., 2011, Phys. Plasmas, 18, 102307
Brandt P. N., Scharmert G. B., Ferguson S., Shine R. A., Tarbell T. D., Title A. M., 1988, Nature, 335, 238
Caroli A., Giannattasio F., Fanfoni M., Del Moro D., Consolini G., Berrilli F., 2015, J. Plasma Phys., 81, 495810514
Chian A. C. L., Rempel E. L., Aulanier G., Schmieder B., Shadden S. C., Welsch B. T., Yeates A. R., 2014, ApJ, 786, 51
Démoulin P., Henoux J. C., Priest E. R., Mandrini C. H., 1996, A&A, 308, 643
Falessi M., Pegoraro F., Schep T., 2015, J. Plasma Phys., 81, 495810505
Giannattasio F., Berrilli F., Biferale L., Del Moro D., Sbragaglia M., Bellot Rubio L., Gošić M., Orozco Suárez D., 2014a, A&A, 569, A121
Giannattasio F., Berrilli F., Consolini G., Del Moro D., Gošić M., Bellot Rubio L., 2018, A&A, 611, A56
Giannattasio F., Del Moro D., Berrilli F., Bellot Rubio L., Gošić M., Orozco Suárez D., 2013, ApJ, 770, L36
Giannattasio F., Stangalini M., Berrilli F., Del Moro D., Bellot Rubio L., 2014b, ApJ, 788, 137
Gošić M., Bellot Rubio L. R., del Toro Iniesta J. C., Suárez D. O., Katsukawa Y., 2016, ApJ, 820, 35
Gošić M., Bellot Rubio L. R., Suárez D. O., Katsukawa Y., del Toro Iniesta J. C., 2014, ApJ, 797, 49
Hadjighasem A., Farazmand M., Blazevski D., Froyland G., Haller G., 2017, Chaos, 27, 053104
Haller G., 2011, Phys. D, 240, 574
Haller G., 2015, Annu. Rev. Fluid Mech., 47, 137
Haller G., Hadjighasem A., Farazmand M., Huhn F., 2016, J. Fluid Mech., 795, 136
Haller G., Yuan G., 2000, Physica D., 147, 352
Hotta H., Iijima H., Kusano K., 2019, Sci. Adv., 5, eeau2307
Iida Y., Hagenaar H. J., Yokoyama T., 2012, ApJ, 752, 149

Iida Y., Yokoyama T., Ichimoto K., 2010, ApJ, 713, 325
Inoue S., Hayashi K., Kusano K., 2016, ApJ, 818, 168
Liu Y., Zhang H., Ai G., Wang H., Zirin H., 1994, A&A, 283, 215
Mathur M., Haller G., Peacock T., Ruppert-Felsot J. E., Swinney H. L., 2007, Phys. Rev. Lett., 98, 144502
Molowny-Horas R., 1994, Sol. Phys., 154, 29
November L. J., Simon G. W., 1988, ApJ, 333, 427
Orozco Suárez D., Katsukawa Y., Bellot Rubio L. R., 2012, ApJ, 758, L38
Orozco Suárez D. et al., 2007a, PASJ, 59, S837
Orozco Suárez D. et al., 2007b, ApJ, 670, L61
Padberg K., Hauff T., Jenko F., Junge O., 2007, New J. Phys., 9, 400
Rempel E. L., Chian A. C.-L., Brandenburg A., 2011, ApJ, 735, L9
Rempel E. L., Chian A. C.-L., Brandenburg A., 2012, Phys. Scr., 86, 018405
Rempel E. L., Chian A. C.-L., Brandenburg A., Muñoz P. R., Shadden S. C., 2013, J. Fluid Mech., 729, 309
Rempel E. L., Chian A. C.-L., Beron-Vera F. J., Haller G., Szanyi S., 2017, MNRAS, 466, L108
Rempel E. L., Gomes T. F. P., Silva S. S. A., Chian A. C.-L., 2019, Phys Rev E, 99, 043206
Requerey I. S., Cobo B. R., Gošić M., Bellot Rubio L. R., 2018, A&A, 610, A84
Rieutord M., Roudier T., Malherbe J. M., Rincon F., 2000, A&A, 357, 1063
Rincon F., Rieutord M., 2018, Living Rev. Sol. Phys., 15, 6
Roudier T., Švanda M., Ballot J., Malherbe J. M., Rieutord M., 2018, A&A, 611, A92
Rutherford B., Dunkerton T. J., Montgomery M. T., 2015, Q. J. Royal Meteorol. Soc., 141, 3344
Schüssler M., 1984, A&A, 140, 453
Shadden S. C., Lekien F., Marsden J. E., 2005, Phys. D., 212, 271
Silva S. S. A., Rempel E. L., Gomes T. F. P., Requerey I. S., Chian A. C.-L., 2018, ApJ, 863, L2
Simon G. W., Weiss N. O., 1989, ApJ, 345, 1060
Steiner O., Rezaei R., 2012, in Golub L., de Moortel I., Shimizu T., eds, ASP Conf. Ser. Vol. 456, Exploring the Active Sun. Astron. Soc. Pac., San Francisco, p. 3
Stenflo J. O., 1973, Sol. Phys., 32, 41
Stenflo J. O., 1975, Sol. Phys., 42, 79
Welsch B. T., Longcope D. W., 2003, ApJ, 588, 620
Yeates A. R., Hornig G., Welsch B. T., 2012, A&A, 539, A1

This paper has been typeset from a TEX/LATEX file prepared by the author.